

# Highly Sensitive, Mechanically Stable Nanopore Sensors for DNA Analysis

By Bala Murali Venkatesan, Brian Dorvel, Sukru Yemenicioglu, Nicholas Watkins, Ivan Petrov, and Rashid Bashir\*

Understanding the biophysics governing single-molecule transport through solid-state nanopores is of fundamental importance in working toward the goal of DNA detection and genome sequencing using nanopore-based sensors. Even with significant advances in semiconductor fabrication technologies, the state-of-the-art in nanopore technology still falls well short of mimicking the elegance and functionality found in biology. Kasianowicz et al.<sup>[1]</sup> pioneered the first in vitro studies of biomolecule transport through single nanopore channels by translocating individual ssDNA and ssRNA molecules through  $\alpha$ -hemolysin protein pores inserted into a lipid bilayer membrane. More recently, focus has shifted to the solid-state domain with numerous groups studying biomolecule transport through solid-state nanopores.<sup>[2–7]</sup> Solid-state nanopores exhibit superior chemical, thermal, and mechanical stability over their biological counterparts, and can be fabricated using conventional semiconductor processes, thereby facilitating mass fabrication and size tunability. They are typically formed in thin  $\text{Si}_3\text{N}_4$  or  $\text{SiO}_2$  membranes using a combination of decompositional ion/electron-beam-based sputtering and surface-tension-driven shrinking processes.<sup>[2,4,7]</sup> Other techniques for creating individual nanopores include the track-etch method for the formation of conical nanopores in polycarbonate membranes.<sup>[8]</sup> The translocation of negatively charged DNA molecules through

these nanometer-sized solid-state pores is conventionally performed using two-terminal electrophoresis, resulting in characteristic blockades in the measured ionic current. This technique has been used to study various physical phenomena at the single-molecule level, including unzipping kinetics of hairpin DNA,<sup>[9]</sup> detection of single-nucleotide polymorphisms,<sup>[10]</sup> stretching transitions in dsDNA,<sup>[11]</sup> biomolecule folding,<sup>[3]</sup> discrimination of long DNA molecules based on length,<sup>[12]</sup> and nanopore-based DNA force spectroscopy.<sup>[13]</sup> Though this technology shows much promise, major hurdles still remain. Fabrication challenges (stress-induced membrane deformation and mechanical failure in  $\text{SiO}_2$  structures),<sup>[5]</sup> limited nanopore lifetime, electrical noise,<sup>[14,15]</sup> and a lack of chemical specificity limit the feasibility of this technology in high-end applications such as DNA sequencing. Thus, there is a need for highly sensitive, mechanically robust nanopore sensors with well-defined surface-charge properties for the detection of specific biological molecules (ssDNA, dsDNA, mRNA).

This paper reports on the development and characterization of a new solid-state nanopore sensor for the detection of single DNA molecules. The  $\text{Al}_2\text{O}_3$  structures reported here exhibit enhanced mechanical properties (increased hardness, decreased stress) and improved electrical performance (low noise, high signal-to-noise ratio) over their  $\text{SiO}_2$  and  $\text{Si}_3\text{N}_4$  counterparts. The fabrication process described results in high device yield and a ten-fold reduction in process time/complexity relative to techniques demonstrated in  $\text{SiO}_2$ .<sup>[5]</sup> High-temperature process steps, wet-etch steps, and electron-beam lithography (EBL) were eliminated, allowing for possible integration with metal electrodes and optical probes.  $\text{Al}_2\text{O}_3$  nanopore sensors fabricated using this process have all the advantages of existing  $\text{SiO}_2$  and  $\text{Si}_3\text{N}_4$  architectures (size control with sub-nanometer precision, controlled contraction/expansion, chemical modification with biomolecules) but also exhibit superior noise performance and increased lifetime over their solid-state counterparts. Interestingly, the formation of nanopores in  $\text{Al}_2\text{O}_3$  membranes resulted in the localized crystallization and faceted grain growth of hexagonal  $\gamma$ - $\text{Al}_2\text{O}_3$  nanocrystallites in the vicinity of the pore, attributed to nanoscale thermal annealing and electron-beam assisted diffusion. This phenomenon has not been reported in  $\text{Si}_3\text{N}_4$  and  $\text{SiO}_2$  topologies, and could potentially enhance the mechanical hardness and localized structure of the nanopore. Bulk membrane properties (crystallinity, composition, and thickness) were studied using transmission electron microscopy (TEM), X-ray photoelectron spectroscopy (XPS), and Auger electron spectroscopy (AES). A 3D symmetric double-cone structure for the nanopore was extracted from conductance

[\*] Dr. R. Bashir, B. M. Venkatesan, B. Dorvel, S. Yemenicioglu, N. Watkins  
Micro and Nanotechnology Laboratory University of Illinois at Urbana  
Champaign, IL 61820 (USA)  
E-mail: rbashir@illinois.edu

Dr. R. Bashir, B. M. Venkatesan, S. Yemenicioglu, N. Watkins  
Department of Electrical and Computer Engineering  
University of Illinois at Urbana  
Champaign, IL 61820 (USA)

B. Dorvel  
Department of Biophysics and Computational Biology  
University of Illinois at Urbana  
Champaign, IL 61820 (USA)

Dr. I. Petrov  
Frederick Seitz Materials Research Laboratory  
University of Illinois at Urbana,  
Champaign, IL 61820 (USA)

Dr. R. Bashir  
Department of Bioengineering  
University of Illinois at Urbana  
Champaign, IL 61820 (USA)

DOI: 10.1002/adma.200803786

measurements, supported by thickness mappings constructed using energy-filtering transmission electron microscopy (EFTEM) methods. The high frequency ( $f > 10$  kHz) noise performance of  $\text{Al}_2\text{O}_3$  nanopores shows an order of magnitude improvement over existing  $\text{Si}_3\text{N}_4$  structures,<sup>[15]</sup> resulting in high sensitivity and exceptional signal-to-noise performance. Finally, the functionality of these  $\text{Al}_2\text{O}_3$ -nanopore sensors is demonstrated through the detection of 5 kbp dsDNA in 1 M KCl by monitoring biomolecule translocation under an applied bias.

The process flow for the fabrication of  $\text{Al}_2\text{O}_3$  nanopores is outlined in Figure 1. A detailed description is provided in the Supporting Information. Atomic layer deposition (ALD) was used to deposit 700 Å of  $\text{Al}_2\text{O}_3$ , confirmed using single-wavelength and spectroscopic ellipsometry. The self-limiting growth characteristic of ALD enables excellent uniformity over large areas, accurate control of film composition and thickness, conformal coating, and high reproducibility, rendering it ideal for membrane applications.<sup>[16]</sup> Plasma-enhanced chemical vapor deposition (PECVD) was used next to deposit 500 nm of low stress silicon nitride (SiN) as a passivation layer to help reduce device capacitance and electrical noise. Optical lithography and RIE were used to pattern 30  $\mu\text{m}$  square membrane regions. A  $\text{CF}_4$ -based etch recipe yielded very high SiN/ $\text{Al}_2\text{O}_3$  etch selectivity (60:1). 300  $\mu\text{m}$  deep, high-aspect-ratio (10:1) Si trenches were next formed on the wafer back side using the Bosch process (deep reactive ion etching tool), with very-high etch selectivity to  $\text{Al}_2\text{O}_3$  (Si/ $\text{Al}_2\text{O}_3$  of 3000:1),<sup>[17,18]</sup> as shown in Figure 2a. Even with significant overetching, a reduction in  $\text{Al}_2\text{O}_3$  thickness of less than 10 nm was observed, resulting in thinned membranes with a final thickness of 60 nm. Nanopores of varying diameter (1–16 nm) were formed in free standing  $\text{Al}_2\text{O}_3$  membranes using a tightly focused electron beam from a JEOL 2010F

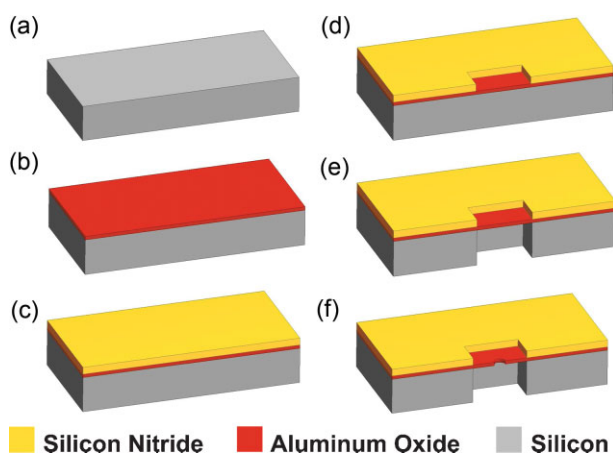


**Figure 1.** Process flow for the formation of  $\text{Al}_2\text{O}_3$  nanopores. a) Start with double-side polished 300  $\mu\text{m}$  thick Silicon wafer. b) Deposit 70 nm of  $\text{Al}_2\text{O}_3$  by ALD. c) Deposit 500 nm low-stress SiN using PECVD process. d) Pattern 30  $\mu\text{m}$   $\times$  30  $\mu\text{m}$  windows on the wafer front side via optical lithography and RIE. e) Pattern 30  $\mu\text{m}$   $\times$  30  $\mu\text{m}$  windows on the wafer backside and etch using DRIE ( $\text{SF}_6 + \text{O}_2$ ), and stop on the  $\text{Al}_2\text{O}_3$  layer creating a membrane. f) Use a tightly focused electron beam to form nanometer-sized pores.

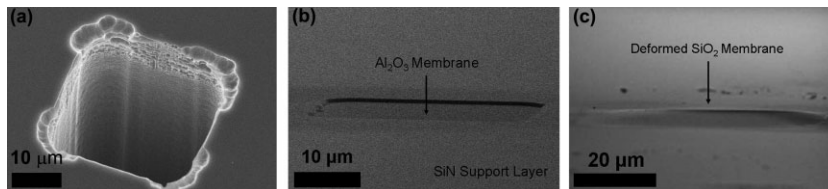


**Figure 2.** a) SEM image of backside trench formed using DRIE. b) SEM cross-section at 5° tilt of  $\text{Al}_2\text{O}_3$  membrane with supporting SiN layer. Membrane is under low tensile stress and appears flat. c) SEM cross-section at 5° tilt of  $\text{SiO}_2$  membrane post-oxidation showing  $\sim 5$   $\mu\text{m}$  vertical deflection over 50  $\mu\text{m}$  span due to high compressive stress. Membrane is significantly deformed resulting in frequent failure.

field-emission-gun transmission electron microscope operated at 200 kV. Decompositional sputtering has been demonstrated in  $\text{SiO}_2$ <sup>[4]</sup> and  $\text{Si}_3\text{N}_4$ <sup>[19,20]</sup> membranes, but has not been previously reported in  $\text{Al}_2\text{O}_3$  material systems.

The precise thickness control and the high etch selectivities achieved using this fabrication process can potentially allow for the formation of ultrathin membranes (thickness  $< 100$  Å). This is particularly useful in forming a solid-state analog to the lipid bilayer (thickness  $\approx 4$ –5 nm),<sup>[1]</sup> an important tool in better understanding the kinetics governing biomolecule transport through proteinaceous pores in cellular membranes. Our low-temperature fabrication process is also compatible with metallization steps, and is applicable to the formation of metal oxide–semiconductor (MOS) capacitors. Simulation work by Gracheva et al.<sup>[21]</sup> on nanopores formed in MOS capacitors with thin  $\text{SiO}_2$  membranes ( $< 5$  nm) reported the possibility of single-nucleotide resolution with potential application to next-generation DNA sequencing systems. This fabrication technique could help enable the possible realization of such structures.

Mechanical stress in the fabricated structures was calculated using Stoney's Law.<sup>[22]</sup> Thermal annealing at 500 °C (30 min) was performed to help relax residual tensile film stress and to improve characteristic film strength.<sup>[23]</sup> Annealing temperatures were kept well below 800 °C, the transition temperature at which sharp increases in film stress were observed for  $t_{\text{film}} > 60$  nm, attributed to phase transitions from the amorphous to the polycrystalline states.<sup>[22]</sup> Katamreddy et al.<sup>[24]</sup> demonstrated that annealing ALD alumina films at 600 °C did not significantly change the amorphous properties of the film. The amorphous structure of these  $\text{Al}_2\text{O}_3$  membranes post-annealing was confirmed by TEM electron diffraction imaging. A low tensile film stress of  $148 \pm 20$  MPa was measured for the composite  $\text{Al}_2\text{O}_3/\text{SiN}$  film stack. Figure 2b is a cross-sectional scanning electron microscopy (SEM) image of a 30  $\mu\text{m}$  square  $\text{Al}_2\text{O}_3$  membrane at a tilt angle of 5° surrounded by a 500 nm thick low stress SiN support layer, imaged using a Hitachi S-4800 microscope. The low tensile film stress results in a flat, mechanically hard membrane region. Figure 2c is a cross-sectional SEM image of a  $\text{SiO}_2$  membrane tilted by 5° post-oxidation. The image illustrates high compressive stress in excess of 300 MPa in the 50  $\mu\text{m}$   $\times$  50  $\mu\text{m}$  membrane region, resulting in significant vertical deflection (5  $\mu\text{m}$  at membrane center), deformation, and bowing. These  $\text{SiO}_2$  structures were formed via thermal wet oxidation at 900 °C of a thin ( $< 100$  nm) Si membrane.<sup>[5]</sup> The thermally induced compressive stress resulted in mechanically brittle  $\text{SiO}_2$

membranes that were prone to frequent rupture/failure during DNA translocation experiments, nanopore functionalization, and nanopore cleaning processes.  $\text{Al}_2\text{O}_3$  membranes were more mechanically robust than their  $\text{SiO}_2$  counterparts, and had increased lifetimes.

Nanopore contraction kinetics depended on initial pore diameter,  $d_{\text{pore}}$ , membrane thickness,  $h$ , and electron-beam intensity. Nanopore contraction was consistently observed upon defocusing the electron beam to an intensity of  $\sim 10^6 \text{ e-nm}^{-2}$  for  $d_{\text{pore}} < h$ . Figures 3a–d show a series of high-resolution TEM (HRTEM) phase-contrast images illustrating the temporal contraction of an  $\text{Al}_2\text{O}_3$  nanopore from an initial diameter of 4 nm to a final diameter of 1 nm. The shot noise in the pore region confirms that the electron beam has completely sputtered through the membrane. The pore quenches in size upon removal of the electron beam. This technique thereby allows for precise tunability and nanometer control over pore dimensions in  $\text{Al}_2\text{O}_3$  membranes. In  $\text{SiO}_2$  and  $\text{Si}_3\text{N}_4$  material systems, nanopore contraction is attributed to thermal decomposition and surface-tension-driven reflow of the amorphous material surrounding the pore.<sup>[4]</sup> Crystallinity is not observed after pore formation, as confirmed by the fast Fourier transform (FFT) of a 4 nm  $\text{Si}_3\text{N}_4$  nanopore (Fig. 3f). In contrast, polycrystalline regions are clearly evident after the formation of  $\text{Al}_2\text{O}_3$  nanopores. Faceted grain growth and the formation of 5–10 nm hexagonal nanocrystallites (i, ii, iii, iv) in the vicinity of  $\text{Al}_2\text{O}_3$  pores are seen in HRTEM images (Fig. 3g), and pairs of diffraction spots are clearly visible in the corresponding FFT (Fig. 3h). The hexagonal nanocrystallites labeled i, ii, iii are not oriented with the zone axis, and thus crystal periodicity is not observed. In contrast, the nanocrystallite labeled iv shows regions of periodicity and clear lattice structure due to its partial alignment with the zone axis. Further examination of these regions revealed a lattice spacing of 2.28 Å (see electron intensity plot in inset of Fig. 3g), corresponding to  $\gamma\text{-Al}_2\text{O}_3$  in its  $\langle 111 \rangle$  crystal orientation. The damage mechanism in alumina during pore formation is attributed to the Knotek–Feibelman oxygen-ion desorption mechanism.<sup>[25,26]</sup> Oxygen is preferentially desorbed

from the surface by core-level ionization processes during electron irradiation, forming high-Al-content regions and faceted metal Al clusters in the vicinity of the pore.<sup>[27]</sup> In ultrahigh-vacuum environments, the reoxidation of these facets is quenched, allowing reactive aluminum to remain in its metallic state, thereby forming stable Al crystals. Metallic Al has a lattice spacing of 2.33 Å in its  $\langle 111 \rangle$  crystal form. In low-vacuum environments, however, as observed in these experiments, the high reactivity of metallic aluminum combined with chamber contamination (molecular oxygen and hydrocarbons) results in reoxidation and the formation of  $\gamma\text{-Al}_2\text{O}_3$  nanocrystallites.<sup>[26]</sup> The nucleation and growth of  $\gamma\text{-Al}_2\text{O}_3$  nanocrystallites is likely due to a combination of thermal annealing and electron-beam-assisted diffusion processes.  $\text{Al}_2\text{O}_3$  nanocrystallites in the more thermostable  $\alpha$  phase (corundum) were not observed. Zywitzki et al.<sup>[28]</sup> showed that intense ion bombardment can hinder the nucleation of the  $\alpha$  phase. Therefore, it is plausible that the use of a high-energy, tightly focused electron beam may also hinder  $\alpha$ -phase nucleation in  $\text{Al}_2\text{O}_3$  thin films. The presence of  $\gamma$ -phase nanocrystallites significantly enhances the mechanical hardness of the local pore region with hardness values expected to range between 20 and 22 GPa.<sup>[28]</sup> This is significantly higher than the mechanical hardness of amorphous  $\text{SiO}_2$  and  $\text{Si}_3\text{N}_4$  pores, thus resulting in mechanically stable  $\text{Al}_2\text{O}_3$ -nanopore sensors suitable for a variety of applications.

Bulk membrane composition was determined using XPS. Strong peaks were seen at binding energies corresponding with core-electron ejections from Al 2s, Al 2p, O 1s, and O 2s orbitals, suggesting that the deposited film contained only Al and O. Ar peaks were attributed to Ar-based sputtering to remove surface carbon contamination prior to analysis. Compositional analysis revealed 37% Al and 63% O, in good agreement with the expected stoichiometric film ratio of 40% Al and 60% O ( $\text{Al}_2\text{O}_3$ ). The XPS spectrum is illustrated in Figure 4a. AES was also used to confirm membrane composition and thickness. The inset of Figure 4a is an Auger differential spectrum showing strong peaks at kinetic energies of 1378 and 503 eV associated with  $kll$  shell transitions for Al and O in the compound  $\text{Al}_2\text{O}_3$  form. Auger results confirm that all residual Si and SiN in the membrane regions were removed by RIE and DRIE processes. This eliminates the possibility that the observed pore crystallinity is the result of unetched, residual Si nanocrystals in the vicinity of the pore. Membrane-depth profiling involving decompositional sputtering and in situ Auger analysis was next done to estimate membrane thickness. 17 Å of material was removed per sputtering cycle using an Ar ion beam, followed by Auger point mode analysis on the membrane region. Peak intensities associated with  $kll$  transitions for Al, O, N (378 eV) and  $lmm$  transitions for Si (92 eV) were measured. Figure 4b illustrates the results of depth profiling. The peak intensities for Si and N are negligible at the collection spot, suggesting the absence of Si and N in or on the membrane. The peak intensities for elemental Al and O are initially very high, but decay rapidly to zero after

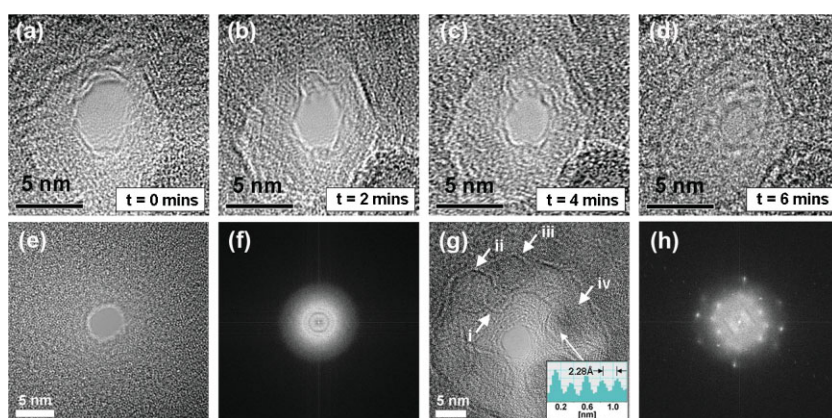


**Figure 3.** a–d) TEM phase-contrast images illustrating temporal contraction of an  $\text{Al}_2\text{O}_3$  nanopore from an initial pore size of  $\sim 4$  nm to a final pore size of  $\sim 1$  nm. e) TEM phase-contrast image of 4 nm  $\text{SiN}$  pore. f) Corresponding FFT showing amorphous structure of  $\text{SiN}$  pore. g) TEM phase-contrast image of a 4 nm  $\text{Al}_2\text{O}_3$  pore. Hexagonal  $\text{Al}_2\text{O}_3$  nanocrystallites are shown by i, ii, iii, iv. iv is partially aligned with the zone axis with 2.28 Å atomic spacing corresponding to  $\gamma\text{-Al}_2\text{O}_3$  in its  $\langle 222 \rangle$  crystal orientation. h) Corresponding FFT showing polycrystalline structure of the pore.

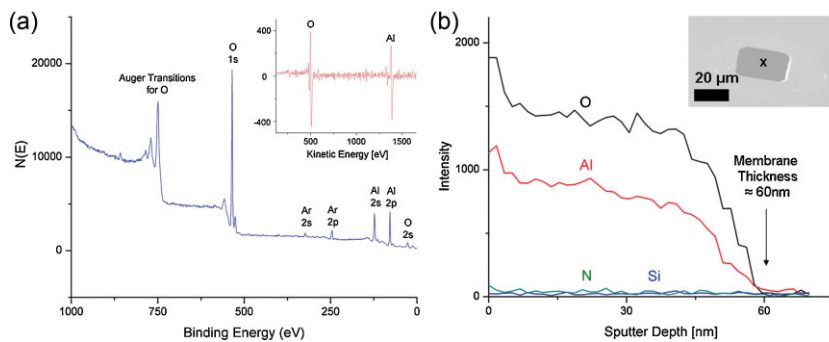


**Figure 4.** a) XPS results on  $\text{Al}_2\text{O}_3$  films. Inset: Auger differential spectra of membrane region postrelease illustrating presence of only Al and O. b) Depth profiling using AES to extract membrane thickness of  $60 \pm 2$  nm. Inset: tilted SEM image of membrane with marked region indicating Auger electron collection region.

35 cycles corresponding to a sputter depth/membrane thickness of  $60 \pm 2$  nm. XPS and AES therefore confirmed the thickness and composition of the membranes in which individual  $\text{Al}_2\text{O}_3$  nanopores were successfully formed.

Nanopore conductance,  $G$ , was measured using current–voltage ( $I$ – $V$ ) measurements at different ionic concentrations, typically 10 mM, 100 mM, and 1 M KCl. Linear  $I$ – $V$  characteristics were seen at each of these molarities in 11 nm diameter pores as illustrated in Figure 5a.  $G$  scaled linearly at high salt concentrations ( $\geq 100$  mM) as expected, and current rectification was not seen in voltage sweeps, suggesting that pore geometry is symmetric. To further probe the performance of  $\text{Al}_2\text{O}_3$  nanopores in electrolyte, the conductance of 11 different nanopores of varying diameter (4–16 nm) were measured in 1 M KCl as shown in Figure 5b. Two geometric models were proposed to fit  $G$ .<sup>[19,29]</sup> The effects of surface charge were neglected in these models, as the Debye screening length given by  $\kappa^{-1}$  (where  $\kappa^2 = 2e^2 n_{\text{KCl}} / k_B T \epsilon \epsilon_0$  in 1 M KCl)  $\ll d_{\text{pore}}$ . At these high salt concentrations, charge carriers in the bulk were expected to dominate current flow. Electro-osmotic flows resulting from counterion condensation on the charged-pore surface should be negligible. The first model<sup>[29]</sup> assumed a purely cylindrical channel of length  $L_{\text{pore}} = 60$  nm with a cross-sectional diameter equal to the pore diameter  $d_{\text{pore}}$  (blue curve of Fig. 5b). The second

conductance model assumed a double-cone structure and accounted for cone angle,  $\alpha$ , and effective channel length,  $h_{\text{eff}}$ .<sup>[19]</sup> Assuming  $\alpha = 30^\circ$  and  $h_{\text{eff}} = h/3$ ,<sup>[19]</sup> an upper conductance bound can be derived (red curve of Fig. 5b). Applying a least squares fit to the measured data (black curve of Fig. 5b), an effective length of  $h_{\text{eff}} \approx 26.5$  nm and cone angle of  $\alpha \approx 24^\circ$  were extracted for  $\text{Al}_2\text{O}_3$  pores, suggesting a double-cone structure. Plasmon imaging using EFTEM confirmed this finding. Plasmons are low-energy-loss events ( $< 50$  eV) occurring due to the longitudinal wave-like oscillations of weakly bound electrons. Most materials produce broad ( $\approx 20$  eV) plasmon peaks, and this low-loss region of the energy-loss spectrum is sensitive to specimen thickness.<sup>[30]</sup> Plasmon

imaging of the pore region was conducted using a JEOL 2010F microscope equipped with a postcolumn imaging filter (GIF by Gatan). A low-loss alumina plasmon peak centered at 30 eV was identified using electron-energy-loss spectroscopy (EELS). The relative thickness profiles of numerous pores were formed by plasmon imaging using an energy loss of 30 eV, energy slit width of 20 eV at an energy resolution of 1 eV. A plasmon image of an 11.1 nm pore is illustrated in the left inset of Figure 5b. This thickness-dependent mapping shows a tapering toward the pore center, which appears dark as electrons traversing the center of the pore undergo minimal inelastic-scattering events (corresponds to zero-loss peak in EELS spectra). In contrast, thick regions induce more inelastic scattering, appearing light in the EFTEM image. Assuming the pore is symmetric based on Current–Voltage ( $I$ – $V$ ) characteristics, the thickness tapering observed strongly suggests an angled double-cone structure. Note in particular that pore geometry and conductance are heavily dependent on material systems, membrane thicknesses and TEM sputtering conditions (spot size and electron dose), as observed by Ho et al. and Smeets et al., who extracted a wide range of cone angles ( $10^\circ$  in 10 nm thick  $\text{Si}_3\text{N}_4$  pores<sup>[20]</sup> and  $45^\circ$  in 60 nm  $\text{SiO}_2/\text{SiN}/\text{SiO}_2$  stacks<sup>[29]</sup>) for different topologies.

The high-frequency noise performance of  $\text{Al}_2\text{O}_3$  nanopores shows significant improvements over existing  $\text{Si}_3\text{N}_4$  technologies.

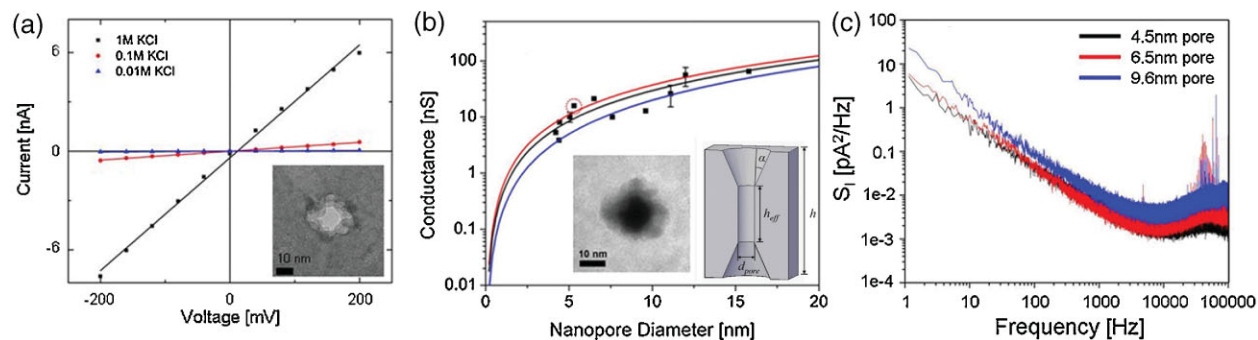


**Figure 5.** a)  $I$ – $V$  characteristics of an 11.1 nm diameter pore measured in 10 mM KCl, 100 mM KCl, and 1 M KCl. Linear  $I$ – $V$  characteristics suggest symmetric pore geometry. b) Pore conductance of 11 nanopores ranging in diameter from 4 to 16 nm. Red and blue lines represent conductance models from literature. Black line is a least-squares fit to the measured data. Predicted geometry of pore from conductance measurements. Left inset: thickness mapping of an 11.1 nm pore constructed using EFTEM. c) Power spectra of three different  $\text{Al}_2\text{O}_3$  nanopores in 1 M KCl at 120 mV. Spectral components at high frequencies ( $f > 1$  kHz) are significantly attenuated relative to  $\text{Si}_3\text{N}_4$  and  $\text{SiO}_2$  systems.<sup>[14,15]</sup>

Noise-power spectra (1 M KCl, 120 mV) for three Al<sub>2</sub>O<sub>3</sub> nanopores of varying diameter (4.5, 6.5, 9.6 nm) are shown in Figure 5c. The low-frequency noise performance of these nanopores is consistent with that observed in Al<sub>2</sub>O<sub>3</sub>-coated Si<sub>3</sub>N<sub>4</sub> structures.<sup>[31]</sup> 1/*f* noise reduction in Al<sub>2</sub>O<sub>3</sub>-coated structures relative to Si<sub>3</sub>N<sub>4</sub> nanopores was attributed to the passivation of nonideal surface properties, including surface charge.<sup>[31]</sup> The process reported here allows for the fabrication of low 1/*f* noise structures in a simple and highly integrated manner. More importantly, high frequency (*f* > 10 kHz) spectral noise components were attenuated by an order of magnitude relative to Si<sub>3</sub>N<sub>4</sub> and Al<sub>2</sub>O<sub>3</sub>-coated Si<sub>3</sub>N<sub>4</sub> structures.<sup>[15,31]</sup> The noise performance is on par with the state-of-the-art in Si<sub>3</sub>N<sub>4</sub> technology reported by Tabard-Cossa et al.<sup>[14]</sup> Noise reduction was attributed to a decrease in device capacitance (measured at 20 ± 5 pF, see Supporting Information, as compared to device capacitance in Si<sub>3</sub>N<sub>4</sub> structures, which were measured in excess of 300 pF.<sup>[15]</sup>), a direct advantage of our reported fabrication process. The result is decreased high-frequency noise, high signal-to-noise ratio, and enhanced sensitivity during DNA translocation experiments. Further enhancements to noise performance could be achieved through device optimization coupled with fluidic isolation techniques using PDMS.<sup>[14]</sup> Noise reduction and characterization is the subject of a future publication. With ongoing research in the reduction of 1/*f* flicker noise through surface passivation techniques, the possibility of single-base resolution using solid-state nanopores could become a reality. Coupled with techniques for imparting chemical selectivity in the nanopore,<sup>[10]</sup> this could be the first step toward a nanopore-based sequencing device.

To demonstrate the functionality of Al<sub>2</sub>O<sub>3</sub> nanopores as biomolecule sensors, dsDNA translocation experiments were performed using 5 kbp dsDNA through 5–5.5 nm diameter nanopores in 1 M KCl at 500 mV. Open-pore conductance was measured through a series of *I*–*V* sweeps prior to the introduction of dsDNA, and results were in good agreement with the proposed conductance model. No translocation events/current blockades were seen prior to the introduction of dsDNA, as shown by the negative control experiment (left inset of Fig. 6a). Upon introduction of 5 kbp dsDNA at a concentration of 6 nM into the *cis* chamber, deep current blockades were observed with excellent signal-to-noise ratio. Figure 6a shows unadjusted current blockade data low-pass-filtered at 100 kHz. The right inset of Figure 6a represents a typical event observed during translocation experiments. The event dwell-time, *t*<sub>D</sub>, the open pore current, *i*<sub>o</sub>, and the blocked pore current level, *i*<sub>b</sub>, are all indicated in the inset. Blockage ratio, *B*<sub>r</sub>, as a function of the cross-sectional diameter of B-form dsDNA (*d*<sub>DNA</sub> = 2.2 nm) and pore diameter is given by Equation 1:

$$B_r(d_{\text{pore}}) = \left( \frac{d_{\text{DNA}}}{d_{\text{pore}}} \right)^2 \quad (1)$$

Measured blockage ratios, *B*<sub>r</sub> = *i*<sub>b</sub>/*i*<sub>o</sub>, versus event dwell-times for *n* = 1178 events are plotted in Figure 6b. A single-blockade level is observed, *B*<sub>r</sub> = 0.20 ± 0.04, with a mode value of 0.17. The results are in excellent agreement with simple geometric arguments that predict *B*<sub>r</sub> = 0.17 (17% of open pore current

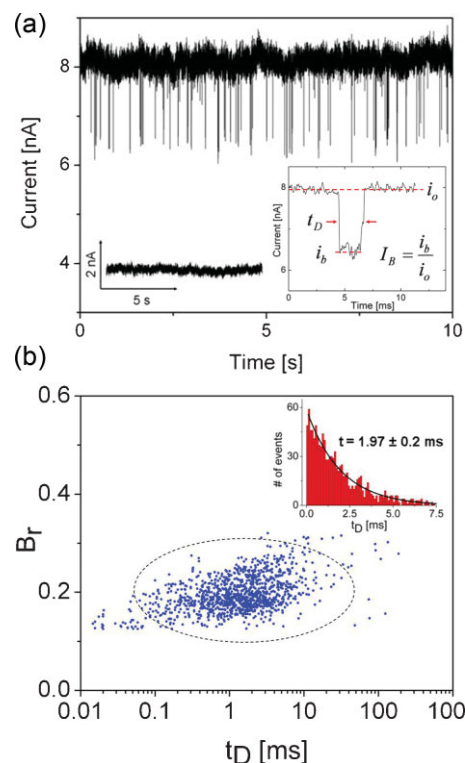


**Figure 6.** a) Typical current blockades seen in a 5.3 nm Al<sub>2</sub>O<sub>3</sub> pore after the addition of 5 kbp dsDNA at a concentration of 6 nM at 500 mV. Data is low-pass filtered at 100 kHz. Left inset: negative control: pore current prior to the introduction of DNA is steady, no blockades are seen. Right inset: typical current blockade with annotations. b) Blockage ratio (*B*<sub>r</sub>) versus event dwell time (*t*<sub>D</sub>) for *n* = 1178 events. Primarily, a single blockade level with *B*<sub>r</sub> = 0.17 is seen. Inset: corresponding event-dwell-time histogram with time constant *t* = 1.97 ± 0.2 ms. Broad dwell-time distribution with large time constant suggests that events are DNA translocations rather than rapid collisions.

blocked) for dsDNA translocating through a 5.3 nm pore. Pore size was chosen to promote unfolded DNA entry, and the absence of secondary populations at higher blockage ratios suggests that the folding of linear 5 kbp dsDNA fragments may not be significant in Al<sub>2</sub>O<sub>3</sub> pores of diameter ≈ 5 nm. Wanunu et al.<sup>[32]</sup> demonstrated the existence of only a single blockade level in Si<sub>3</sub>N<sub>4</sub> pores of diameter 4 nm using 8 kbp dsDNA. The inset of Figure 6b is a dwell-time histogram with *t*<sub>p</sub> denoting the peak location (most probable translocation time), where *t*<sub>p</sub> = 200 μs. A monoexponential decay function with a time constant of *t* = 1.97 ± 0.2 ms is fitted to the dwell-time distribution. As the vast majority of events are spread over the tail of the distribution, the mean dwell time (*μ* = 3.73 ms) is heavily weighted by the time-constant *t* rather than short events (*t*<sub>D</sub> < *t*<sub>p</sub>). The fitted time constant is in good agreement with timescales associated with DNA translocation in Si<sub>3</sub>N<sub>4</sub> pores of similar size (~4 nm) using 6 kbp dsDNA fragments in 1 M KCl.<sup>[32]</sup> These slow time scales suggest that the majority of current blockades observed are indeed DNA-translocation events involving significant interactions with the pore surface, as opposed to DNA collisions (rapid interaction without translocation), which typically have been shown to occur on much faster time scales of the order of *τ* ≈ 100 μs.<sup>[32]</sup>

In summary, this work presents the development and characterization of highly sensitive, mechanically robust,  $\text{Al}_2\text{O}_3$  nanopores for DNA detection. The process described achieves high yield, greatly reduces fabrication complexity, and results in structurally robust, low noise platforms for single-molecule analysis.  $\text{Al}_2\text{O}_3$ -nanopore sensors have all the advantages of existing  $\text{SiO}_2$  and  $\text{Si}_3\text{N}_4$  architectures (size control with sub-nanometer precision, chemical modification, and attachment of organosilanes) but also exhibit superior noise performance and increased lifetime over their solid-state counterparts. An order of magnitude reduction in high-frequency noise ( $f > 10$  kHz) was observed relative to  $\text{Si}_3\text{N}_4$  structures. Interestingly, a new phenomenon was witnessed during nanopore formation, that is, the localized crystallization and faceted-grain growth of hexagonal  $\gamma$ - $\text{Al}_2\text{O}_3$  nanocrystallites in the vicinity of the nanopore. The nucleation and growth of  $\gamma$ -phase nanocrystallites was attributed to thermal annealing and electron-beam-assisted diffusion, thereby enhancing the local hardness of the nanopore. Finally, the detection of single molecules using this new architecture was demonstrated (5 kbp dsDNA) with signal-to-noise performance being on par with the state-of-the-art in solid-state nanopore technology. Results suggest that nanopores in high  $k$ -dielectric materials, such as  $\text{Al}_2\text{O}_3$ , with unique surface properties, indeed function as highly sensitive biomolecule-detection platforms, an alternative to well-established  $\text{SiO}_2$  and  $\text{Si}_3\text{N}_4$  systems. This technology serves as a template to further explore the physics governing DNA transport. Such studies provide fundamental insight into the mechanisms driving biological processes, including cell signaling and regulation using gated, selective ion channels, RNA translation using nuclear membrane pores, protein secretion across cellular membranes, and viral infection by phages. This technology finds broad application in bio-nanotechnology.

### Acknowledgements

We thank the staff at Micro and Nanotechnology Lab, UIUC (Yaguang Lian, Edmond Chow) for their assistance and R. Haasch and C. Lei at Frederick Seitz Materials Research Lab (MRL), UIUC for help with XPS, AES, and TEM work. We thank Dr. C. Dekker's research group for help with the design of the PMMA flow cell. We also thank Dr. A. Meller's research group, particularly M. Wanunu for discussions relating to DNA translocation experiments. We acknowledge the funding from the National Institutes of Health through the NIH Roadmap for Medical Research Nanomedicine Development Center (PN2 EY 018230) and NIH R21 EB007472. Supporting Information is available online from Wiley InterScience or from the author.

Received: December 22, 2008

Revised: February 6, 2009

Published online:

- [1] J. J. Kasianowicz, E. Brandin, D. Branton, D. W. Deamer, *Proc. Natl. Acad. Sci. USA* **1996**, *93*, 13770.
- [2] J. Li, D. Stein, C. McMullan, D. Branton, M. J. Aziz, J. A. Golovchenko, *Nature* **2001**, *412*, 166.
- [3] J. Li, M. Gershow, D. Stein, E. Brandin, J. A. Golovchenko, *Nat. Mater.* **2003**, *2*, 611.
- [4] A. J. Storm, J. H. Chen, X. S. Ling, H. W. Zandbergen, C. Dekker, *Nat. Mater.* **2003**, *2*, 537.
- [5] H. Chang, F. Kosari, G. Andreadakis, M. A. Alam, G. Vasmatzis, R. Bashir, *Nano Lett.* **2004**, *4*, 1551.
- [6] J. B. Heng, C. Ho, T. Kim, R. Timp, A. Aksimentiev, Y. V. Grinkova, S. Sligar, K. Schulten, G. Timp, *Biophys. J.* **2004**, *87*, 2905.
- [7] M. J. Kim, D. C. Bell, A. Meller, *Adv. Mater.* **2006**, *18*, 3149.
- [8] C. C. Harrell, S. S. Zuzanna, C. R. Martin, *Small* **2006**, *2*, 194.
- [9] B. McNally, M. Wanunu, A. Meller, *Nano Lett.* **2008**, *10*, 3418.
- [10] S. M. Iqbal, D. Akin, R. Bashir, *Nat. Nano* **2007**, *2*, 243.
- [11] J. B. Heng, A. Aksimentiev, C. Ho, P. Marks, Y. V. Grinkova, S. Sligar, K. Schulten, G. Timp, *Nano Lett.* **2005**, *5*, 1883.
- [12] A. J. Storm, C. Storm, J. Chen, H. Zandbergen, J.-F. Joanny, C. Dekker, *Nano Lett.* **2005**, *5*, 1193.
- [13] U. F. Keyser, B. N. Koeleman, S. van Dorp, D. Krapf, R. M. M. Smeets, S. G. Lemay, N. H. Dekker, C. Dekker, *Nat. Phys.* **2006**, *2*, 473.
- [14] V. Tabard-Cossa, D. Trivedi, M. Wiggan, N. N. Jetha, A. Marziali, *Nanotechnology* **2007**, *18*, 305505.
- [15] R. M. M. Smeets, U. F. Keyser, N. H. Dekker, C. Dekker, *Proc. Natl. Acad. Sci.* **2008**, *105*, 417.
- [16] W.-K. Kim, W.-H. Nam, S.-H. Kim, S.-W. Rhee, *J. Chem. Eng. Jpn.* **2005**, *38*, 578.
- [17] S. Jensen, A. D. Ren Yal Inkaya, S. Jacobsen, T. Rasmussen, F. E. Rasmussen, O. Hansen, *Phys. Scripta* **2004**, *T114*, 188.
- [18] K. R. Williams, R. S. Muller, *J. Microelectromech. Syst.* **1996**, *5*, 256.
- [19] M. J. Kim, B. M. K. Murata, A. Meller, *Nanotechnology* **2007**, *20*, 205302.
- [20] C. Ho, R. Qiao, J. B. Heng, A. Chatterjee, R. J. Timp, N. R. Aluru, G. Timp, *Proc. Natl. Acad. Sci. USA* **2005**, *102*, 10445.
- [21] M. E. Gracheva, A. Xiong, A. Aksimentiev, K. Schulten, G. Timp, J.-P. Leburton, *Nanotechnology* **2006**, *17*, 622.
- [22] G. Krauthaim, T. Hecht, S. Jakschik, U. Schröder, W. Zahn, *Appl. Surf. Sci.* **2005**, *252*, 200.
- [23] H. Fischer, M. Hemelik, R. Telle, R. Marx, *Dent. Mater.* **2005**, *21*, 671.
- [24] R. Katamreddy, R. Inman, G. Jursich, A. Soulet, A. Nicholls, C. Takoudis, *Thin Solid Films* **2007**, *515*, 6931.
- [25] S. D. Berger, I. G. Salisbury, R. H. Milne, D. Imeson, C. J. Humphreys, *Philos. Mag. B* **1987**, *55*, 341.
- [26] J. E. Bonevich, L. D. Marks, *Ultramicroscopy* **1991**, *35*, 161.
- [27] M. Kundu, N. Miyata, M. Ichikawa, *Appl. Phys. Lett.* **2001**, *79*, 842.
- [28] O. Zywitzki, K. Goedicke, H. Morgner, *Surf. Coat. Technol.* **2002**, *151–152*, 14.
- [29] R. M. M. Smeets, U. F. Keyser, D. Krapf, M.-Y. Wu, N. H. Dekker, C. Dekker, *Nano Lett.* **2006**, *6*, 89.
- [30] D. R. G. Mitchell, X. Wang, R. A. Caruso, *Micron* **2008**, *39*, 344.
- [31] P. Chen, T. Mitsui, D. B. Farmer, J. Golovchenko, R. G. Gordon, D. Branton, *Nano Lett.* **2004**, *4*, 1333.
- [32] M. Wanunu, J. Sutin, B. McNally, A. Chow, A. Meller, *Biophys. J.* **2008**, *95*, 1.